Journal of Marine Research, 66, 563–588, 2008

Journal of
MARINE RESEARCH

Volume 66, Number 5

Turbulence and boluses on an internal beach

by Daniel Bourgault[1], Dan E. Kelley[2] and Peter S. Galbraith[3]

ABSTRACT

In a manner similar to that of surface waves on beaches, high-frequency interfacial waves (IWs) may break when approaching the 'internal coastline,' where the undisturbed pycnocline intersects the shoaling bottom. This process has been studied previously in idealized laboratory and numerical experiments but there are few field observations to document the properties of IWs shoaling on natural internal beaches. This paper presents observations of currents, density and turbulence collected inshore of the break point of an internal beach of the St. Lawrence Estuary. A series of large- and small-amplitude complex-shaped and unorganized internal boluses was observed. The structure of these boluses is discussed, along with their role in boundary turbulence and transport.

1. Introduction

By extrapolating Michallet and Ivey's (1999) laboratory results on the mixing properties of shoaling interfacial waves (IWs) to field situations, Bourgault and Kelley (2003) argued that the breaking of large-amplitude IWs on internal beaches, although sporadic and localized to narrow internal swash zones, may be significant to the overall mixing budget in the St. Lawrence Estuary. Given the widespread occurrences of IWs in environments such as bays, fjords, gulfs, lakes, and shelves (Jackson, 2004), boundary mixing induced by breaking IWs on internal beaches may be significant to coastal systems in general.

After the breaking of an IW on an internal beach, a series of up-slope propagating pulse-like features, referred as internal boluses, may be produced. Such boluses have been studied

1. Department of Physics and Physical Oceanography, Memorial University, St. John's, NL, A1B 3X7, Canada. ***email: daniel.bourgault@mun.ca***
2. Department of Oceanography, Dalhousie University, Halifax, Nova Scotia, B3H 4J1, Canada.
3. Ocean and Environmental Science Branch, Maurice-Lamontagne Institute, Department of Fisheries and Oceans Canada, Mont-Joli, Quebec, G5H 3Z4, Canada.

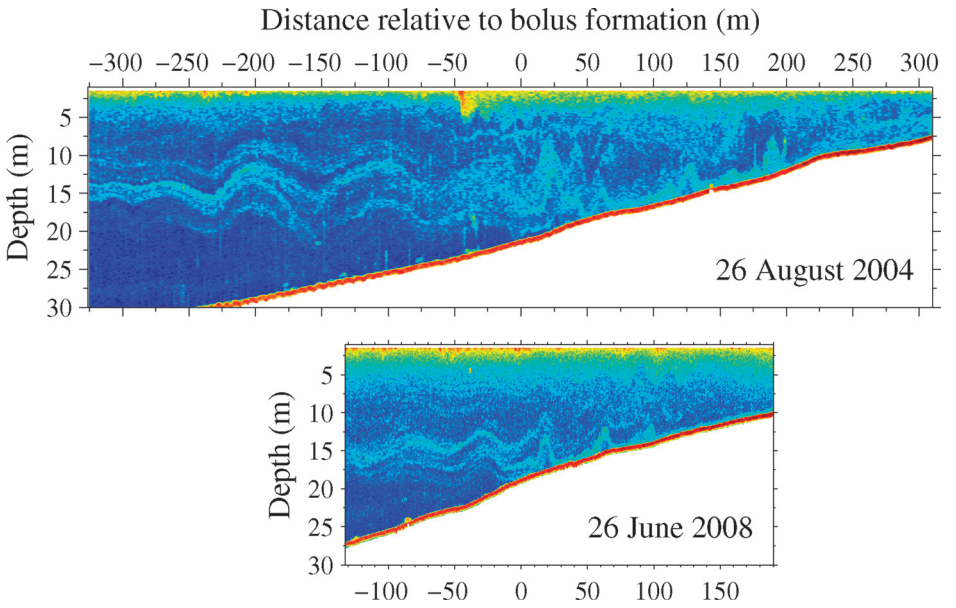

Figure 1. Echograms showing the transformation of shoaling internal wavetrains into series of up-slope propagating boluses on the slope of Ile-aux-Lièvres in the St. Lawrence Estuary. (top) Observations made by Bourgault *et al.* (2007) between 1457 UTC and 1501 UTC on 26 August 2004, i.e. 4.8 hours after the time of low water at Pointe-au-Père, along the transect labeled '2004' in Figure 2.(bottom) New observations collected between 2252 UTC and 2256 UTC on 26 June 2008, i.e. 4.4 hours after the time of low water at Pointe-au-Père, along the transect labeled '2008' in Figure 2.

in the laboratory for the idealized situation of IWs normally incident onto uniform and smooth slopes in otherwise quiescent fluids (Wallace and Wilkinson 1988; Helfrich: 1992). However, their existence, properties and role in boundary mixing in natural environments is not well documented. Recently, Bourgault *et al.* (2007) reported field observations of the complete up-slope evolution, from generation to disappearance, of an internal bolus produced by an IW propagating orthogonally to a vertically sheared current and normally incident on a quasi-uniform, sandy-muddy internal beach (Fig. 1). The bolus observed in the field showed remarkable similarities to the laboratory ones, despite the differences between the idealized laboratory and complex natural environments. In particular, the aspect ratio of the natural bolus, i.e. $(a/L_b)_{\text{field}} = 0.28 \pm 0.02$, where a is the bolus vertical displacement and L_b the length of its base, was constant throughout the upslope progression and within the range observed in the laboratory $(a/L_b)_{\text{lab}} = 0.3 \pm 0.1$ (Wallace and Wilkinson 1988; Helfrich, 1992).

Intrigued by the role that boluses may play in boundary mixing, but without *in situ* turbulence measurements, Mirshak (2008) re-examined the 2004 field observations of Bourgault *et al.* (2007) in the context of the theory developed by Wallace and Wilkinson (1988) for

the evolution of decaying boluses. The result of this exercise indirectly suggests that the natural boluses produce little mixing. Mirshak (2008) hypothesized that the most significant mixing associated with shoaling IWs occurs near the breaking depth (Vlasenko and Hutter, 2002) rather than during the run-up/run-down phase.

Motivated by this hypothesis, we conducted in August 2006 an exploratory field survey to measure turbulence through boluses at two sites, *A* and *B*, along the flank of an island in the St. Lawrence Estuary (Fig. 2). Site *A* was chosen because *in situ* measurements collected in 2002 (Bourgault *et al.*, 2005) and 2004 (Bourgault *et al.*, 2007; Mirshak, 2008) revealed that it is within an area exposed to periodic occurrences of normally incident shoaling boluses. Furthermore, preliminary observations collected in 2008 near site *A* show striking similarities with the 2004 observations in terms of timing, spatial structures and scales of the shoaling IWs and boluses (Fig. 1). Together these observations suggest that shoaling internal waves is an integral aspect of the physical oceanography of this environment. Site *B* was chosen because prior work with shore-based and aerial imagery of sea-surface patterns

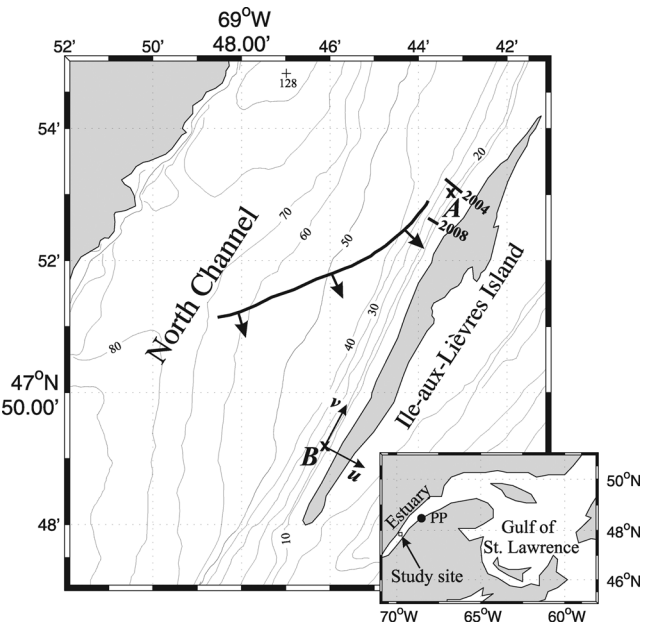

Figure 2. Bathymetric chart of the research area. The crosses indicate the sampling sites *A* and *B* where turbulence measurements presented in this study were collected. The curved solid line and associated vectors indicate the internal wavetrain front position and propagation direction as previously observed from shore-based and aerial photogrammetry by Bourgault and Kelley (2003). The straight solid lines, labeled '2004' and '2008', are the transects along which the echograms presented in Figure 1 were collected. The letters PP in the inset indicate the Pointe-au-Père tidal gauge.

(Bourgault and Kelley, 2003) suggested that IWs shoal obliquely there (see wavefront curve on Fig. 2). We report here the results of this field survey and discuss the impact of internal boluses on up-slope transport, bottom drag and boundary turbulence.

2. Methods

a. Sampling

Wave-induced boundary processes were examined at two sites, denoted *A* (47°53.03 N, 69°43.27 W) and *B* (47°49.21 N, 69°46.13 W), both in water depths $H = 18 \pm 1$ m, along the flank of Ile-aux-Lièvres Island in the St. Lawrence Estuary (Fig. 2). Sampling was carried out during calm wind conditions from an anchored 8-m boat that maintained its position to within ±50 m of a station. Measurements were collected between 1537 Universal Time Coordinated (UTC) and 1853 UTC on 8 August 2006 at site *A* and between 1528 UTC and 1851 UTC on 9 August 2006 at site *B*. Relative to the M_2 tide, these periods correspond to a time when internal boluses are most expected, i.e. between 2 and 6 hours after the time of low water at Pointe-au-Père (Bourgault and Kelley, 2003; Bourgault *et al.*, 2005; Mirshak, 2008).

Finescale flow visualization and three-dimensional current profiles were obtained at site *B* with a Workhorse 600 kHz acoustic Doppler current profiler (ADCP) manufactured by RD Instruments. The pinging and record rates were 1 Hz; i.e., there was no ensemble averaging, and the vertical bin size was 0.2 m. As recommended by the manufacturer for this 20° beam angle ADCP, the data acquired in the bottom 6% of the water column, which corresponds to roughly 1 m at the sampling site, were rejected due to potential side-lobe contamination (RDI Instruments, 1996). The velocity vectors were recorded in earth geographic coordinates. However, to simplify the interpretation of the measurements, the horizontal velocity vectors were afterward rotated clockwise by 28° to provide across- u and along-shore v components (Fig. 2).

Profiles of pressure, temperature, conductivity and vertical shear were collected at both sites *A* and *B* with a free-fall, loosely-tethered, coastal vertical microstructure profiler (VMP) manufactured by Rockland Scientific International (RSI). The VMP is equipped with a Seabird SBE-3F temperature sensor, an unpumped SBE-4C conductivity sensor, a SBE-7 microstructure conductivity sensor, two Thermometrics fast-response FP07 thermistors, and two RSI SPM-38-1 airfoil shear probes. The shear probes were mounted orthogonally to each other in order to measure two components of the vertical shear. Microstructure conductivity, temperature and shear were sampled at 512 Hz while all other quantities were sampled at 64 Hz. We refer the reader to Moum *et al.* (1995), Gregg (1999), Lueck *et al.* (2002) and Macoun and Lueck (2004) for historical perspectives and details on the characteristics of such turbulence profilers and the sensors they carry.

In total, 193 VMP profiles were collected at site *A* and 183 at site *B*, providing on average one profile every 60 s. The start time of each profile is indicated with the | symbol on top of

Figures 4, 6 and 7. Averaged over all profiles collected in this experiment, the fall speed and standard deviation of the VMP was $\overline{w}_{\mathrm{vmp}} = 0.60 \pm 0.05\ \mathrm{m\,s^{-1}}$, information used below for the calculation of dissipation rates. In order to prevent damaging the sensors, the casts were stopped a few meters above the bottom.

Towed echosounder measurements were not collected during this field survey. Consequently, there is no coincident information available on the spatial structures of the internal wave/bolus fields, only time series at sites *A* and *B*. Our measurements are interpreted under the assumption that the phenomena depicted in Figure 1 are representative of the conditions that prevailed at both sites while sampling was carried out.

b. Data reduction

To reduce random noise, the raw ADCP current measurements were low-pass filtered in time and in vertical space using a fourth-order Butterworth filter with cutoff frequency 1/10 Hz and wavenumber 1/2 cpm. This reduced the statistical uncertainty of u, v and w to $\pm 0.01\ \mathrm{m\,s^{-1}}$ (95% CI). The velocities were then decimated on a 10 s $\times$ 0.2 m regular grid. Low- (U, V, W) and high-frequency (u', v', w') currents were obtained with low- and high-pass filters of cutoff frequency 1/1500 Hz. This cutoff frequency is roughly three times lower than the median buoyancy frequency (see Eq. 1) measured during the experiment.

Water density was computed from the equation of state of seawater (Gill, 1982) given the salinity, inferred from the SBE-4C conductivity measurements (Lewis and Perkin, 1978), and the SBE-3F temperature measurements. For plotting and two-dimensional (time-depth) interpolation purposes, the raw density measurements σ_t' were sorted to remove overturns (Thorpe, 1977) and averaged into 1-m vertical bin size to produce the variable σ_t.

The buoyancy frequency

$$N^2 = -\frac{g}{\rho_0}\frac{\partial \overline{\sigma}_t}{\partial z}, \tag{1}$$

was calculated using centered differences, where $\overline{\sigma}_t$ represents the density data that have been filtered in the vertical with cutoff wavenumber 1/2 cpm to match the velocity filter, $\rho_0 = 1015\ \mathrm{kg\,m^{-3}}$ is a reference density, $g = 9.81\ \mathrm{m\,s^{-2}}$ the gravitational acceleration, and z the upward axis.

From the microstructure shear measurements, the dissipation rate of turbulent kinetic energy per unit mass ϵ, in $\mathrm{W\,kg^{-1}}$, was calculated over 1-m vertical bin sizes following standard procedures (Oakey and Elliott, 1982; Wesson and Gregg, 1994; Moum *et al.*, 1995; Peters, 1997). Such dissipation measurements are generally accepted to be accurate to within a factor of 2 (Oakey, 1982).

However, one precaution needed to be taken in our dissipation calculations. Shear measurements depend on the flow speed w_p past the probes (Macoun and Lueck, 2004). This speed is generally assumed to be equal to the fall speed of the profiler w_{vmp} which is inferred

by differentiating the pressure measurements with respect to time. As pointed out by Klymak and Gregg (2004), this method does not accurately reflect the flow speed past the probe if the sampling is carried out through phenomena that are characterized by vertical velocities comparable to w_{vmp}. Klymak and Gregg (2004) minimized this error by assuming that their profiler fell at a predictable speed $\overline{w}_{\text{vmp}}(z)$ equal to the mean, for a given depth, of all profiles collected in their experiment. In cases where the fall rate of a given profile and at a given depth deviated from the mean by more than 1.5 standard deviations, they used $w_p = \overline{w}_{\text{vmp}}$ instead of using the recorded speed. We applied this method to the measurements collected at site *A*. For site *B*, we made use instead of the concomitant ADCP measurements and the flow past the shear probes was calculated as

$$w_p = w_{\text{vmp}} + w_i, \tag{2}$$

where w_i is the vertical velocity measured from the ADCP (i.e. w as reduced above) and bi-linearly interpolated at the depth and time of the VMP measurements.

The density σ_t, buoyancy frequency squared N^2 and dissipation ϵ measurements were then bi-linearly interpolated on a 10 s $\times$ 0.2 m regular grid coincident with the reduced current measurements.

The Richardson number was calculated from the interpolated fields as

$$\text{Ri} = \frac{N^2}{S^2}, \tag{3}$$

where

$$S^2 = \left(\frac{\partial u}{\partial z}\right)^2 + \left(\frac{\partial v}{\partial z}\right)^2, \tag{4}$$

is the fine-scale vertical shear squared estimated using centered differences. Given the vertical filter applied to both (u, v) and $\overline{\sigma}_t$, this can be considered a 2-m scale Richardson number. The Richardson number is used here to indicate stability of the water column. Linear theory indicates that the flow is dynamically unstable when $\text{Ri} < 1/4$ (Miles, 1961; Kundu and Cohen, 2004) but this criterion can be difficult to apply strictly to field observations due to resolution limits of instrumentation (e.g. Moum *et al.* (2003)). For this reason, we interpret Ri more as a qualitative indicator of the stability of the water column. Note also that in the figures tanh(Ri) is presented instead of Ri. This is a convenient way to visually highlight low Ri regions since, rounded to two figures, $\tanh(\text{Ri}) = \text{Ri}$ for $\text{Ri} \leq 1/2$ and $\lim_{\text{Ri}\to\infty} \tanh(\text{Ri}) = 1$.

The turbulent dissipation rate per plan area, in W m^{-2}, was calculated as

$$\mathcal{E} = \int_{z_1}^{z_2} \rho\epsilon \, dz, \tag{5}$$

where z_1 and z_2 are the depths of the deepest and shallowest measurements for a given profile. Since turbulence measurements were not generally obtained down to the bottom,

where the dissipation may be expected to be the largest due to bottom friction, the $\mathcal{E}$ values must be regarded as lower bounds.

The magnitude of the bottom stress was parameterized as

$$\tau_b = \rho_0 C_D \left(u_b^2 + v_b^2\right), \tag{6}$$

where $\rho_0 = 1017\ \mathrm{kg\,m^{-3}}$, u_b and v_b are near-bottom horizontal velocities and C_D is a bottom drag coefficient (Gill, 1982). Lacking direct turbulence measurements in the bottom-boundary layer of this environment to infer the drag coefficient, we used the value of $C_D = 3.1 \times 10^{-3}$ reported by Geyer *et al.* (2000) as representative of sandy-muddy bottom conditions in a partially-mixed estuary. The velocities u_b and v_b are taken at 3.5 m above the bottom (Geyer *et al*., 2000).

Two lengthscales were used in this study to characterize the vertical scale of turbulent overturns. The first is the Ozmidov scale (Ozmidov, 1965) defined as

$$L_O = \left(\frac{\epsilon}{N^3}\right)^{1/2}. \tag{7}$$

Near the bottom boundary layer where the dissipation can be large and the stratification low, unphysically large values of L_O can arise. In order to avoid biasing statistical analysis due to these outliers, values of L_O greater than the total water depth H are disregarded from the analysis, which represents 2% of the samples.

The second is the Thorpe scale (Thorpe, 1977; Dillon, 1982) defined as

$$L_T = < d^2 >^{1/2}, \tag{8}$$

where d is the Thorpe displacement defined as the distance required to re-arrange each measurements within the raw density profile σ_t', which may contain density overturns, into a gravitationally stable profile. This re-arrangement is done by sorting σ_t' into descending order. The symbol $< >$ denotes an averaging operator normally applied to individual overturns identified in a given profile (Galbraith and Kelley, 1996; Gargett and Garner, 2008). Here, we take the averaging operator $< >$ to include all overturning signals within the water column, i.e. signals for which $|d| > 0$. Portions of the water column where $d = 0$ are interpreted as being gravitationally stable and are not taken into account in the calculation of the Thorpe scale. In this study we do not examine individual overturns but the averaged overturning signal within the water column. Thorpe scales that are less than 5 times the vertical resolution δz of the fine-scale measurements are disregarded from the analysis (Galbraith and Kelley, 1996). In Section 3a quantitative comparison is made between L_T and $< L_O >$.

For visual comparison purposes with the other 1-m binned variables (e.g. ϵ, L_O), we also computed a displacement scale taken as

$$L_d = \overline{d^2}^{1/2}, \tag{9}$$

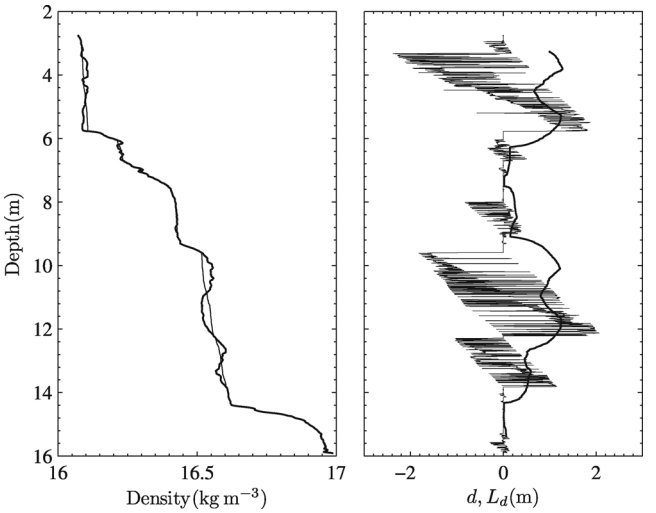

Figure 3. Example of overturning signals observed at 1606 UTC at site *B*. (left) The thick and thin lines are, respectivelty, the raw σ_t' and re-ordered density profiles. (right) The thin and thick lines are, respectively, the Thorpe displacements d and displacement scale L_d.

where the overbar is a 1-m averaging operator applied to all values of d, including $d = 0$ cases. The displacement scale L_d is then bi-linearly re-interpolated on the same $10\,\mathrm{s} \times 0.2\,\mathrm{m}$ regular grid onto which previous variables were interpolated. Figure 3 shows an example of these overturning scales from a typical profile collected at site *B*.

The Ozmidov scale can only be computed from the microstructure measurements while the Thorpe scale can in principle be computed from more standard fine-scale CTD measurements. Relationships have been found between L_O and L_T in the seasonal thermocline (Dillon, 1982) and estuaries (Peters, 1997) and have been used to infer dissipation ϵ from fine-scale measurements alone (e.g. Klymak and Gregg (2004)).

3. Results

a. Observations at site A

The observations collected at site *A* with the turbulence profiler alone are presented in Figure 4. Around 22 ± 2 irregularly-spaced bolus-like features are observed, identified by local maxima in the vertical displacement of the interfacial isopycnal $\rho_s = 1016.0\,\mathrm{kg\,m^{-3}}$ (white contour line on Fig. 4)). They have timescales $100 \leq \tau \leq 300\,\mathrm{s}$, vertical displacement $2 \leq a \leq 10$ m and near-bottom density variation $2 \leq \Delta\sigma_t \leq 4\,\mathrm{kg\,m^{-3}}$. Relative to the total water depth at the sampling site $H \approx 18$ m, the boluses have normalized vertical displacement $0.1 \leq a/H \leq 0.7$.

The mean dissipation at site *A* (Fig. 4) is $\bar{\epsilon}_A = 3 \times 10^{-6} (3 \times 10^{-8}, 2 \times 10^{-5})\,\mathrm{W\,kg^{-1}}$, where the numbers in parenthesis represent the 2.5% and 97.5% percentiles of the distribution. The ϵ_A signal displayed a complex and patchy pattern, with orders of magnitude

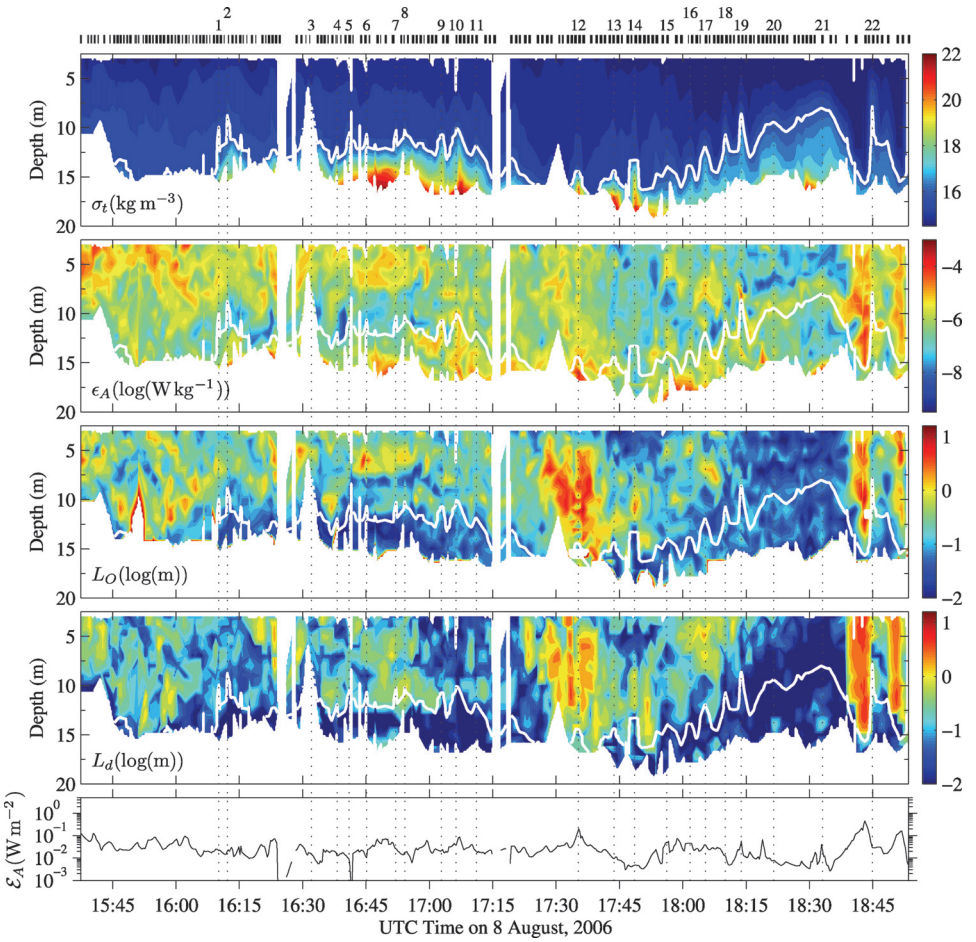

Figure 4. Observations of boundary processes at site *A*. Space-time contours of the (first) density σ_t, (second) dissipation rate of turbulent kinetic energy ϵ_A, (third) Ozmidov scale L_O, (fourth) displacement scale L_d and (bottom) time series of the area density dissipation rate $\mathcal{E}_A$. The white countour line in each panel is the isopycnal used for visually inferring bolus-like features (i.e. $\sigma_t = 16.0$ kg m^{-3}). The | symbols on top of the first panel indicate the timing of each VMP cast. The vertical dotted lines are visual aids to help relate the observations to the identified boluses, numbered from 1 to 16 above the top panel.

variations over scales of ∼1 m and ∼100 s. There is no striking visual correspondence between the dissipation field ϵ_A and isopycnal displacements.

Qualitatively, there is a visual correspondence between the Ozmidov L_O and displacement L_d scales (Fig. 4). It will be shown below that such a visual correspondence also appears in the observations collected at site *B*. The quantitative relationship between Ozmidov and Thorpe scales is examined in the following section by combining both sets of

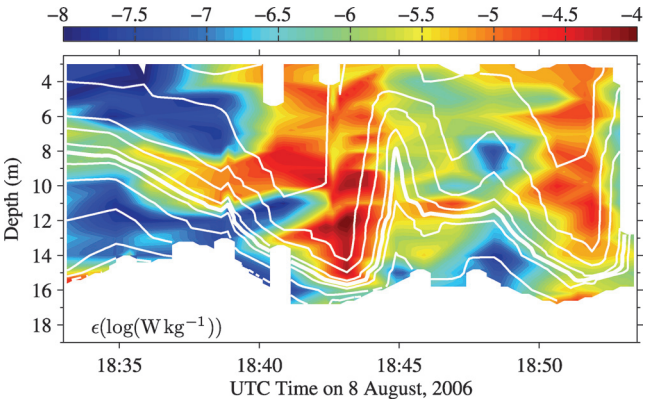

Figure 5. Details of the isopycnal displacements and dissipation around bolus 22 of Figure 4. The white lines are density countours, 0.4 kg m^{-3} apart, and the thick white line is the $\sigma_t = 16.0$ kg m^{-3} contour.

measurements. The mean Ozmidov scale is $\overline{L}_O = 1(0.06, 6)$m and is comparable to the mean displacement scale $\overline{L}_d = 0.8(0.02, 3)$m.

Over the sampling period, $\overline{\mathcal{E}}_A \geq 0.06(0.008, 0.2)$ W m^{-2} (we use the inequality symbol $\geq$ since measurements were not collected down to the bottom and $\overline{\mathcal{E}}_A$ is therefore a lower bound). Here again, there is no obvious correspondence between bolus occurrences, identified with the vertical dotted lines, and peaks in $\mathcal{E}_A$ (Fig. 4). A few boluses seem coincident with local maxima in $\mathcal{E}_A$ (e.g. boluses 12, 19 and 21) but others seem coincident with local minima in $\mathcal{E}_A$. For example, a closer inspection at the dissipation fields (ϵ_A and $\mathcal{E}_A$) and lengthscales fields (L_O and L_d) around bolus 22 suggests that the arrival of this large-amplitude bolus suppresses the turbulence and reduces the depth-integrated dissipation $\mathcal{E}_A$ by more than an order of magnitude, perhaps by bringing more stratification than vertical shear throughout the water column. Figure 5 shows the dissipation rates around bolus 22 in greater detail.

b. Observations at site B

i. General. Figures 6 and 7 display the more comprehensive set of observations collected at site *B* with the turbulence profiler and concomitant ADCP measurements. Around 27 ± 2 boluses were identified visually as either local maxima in backscatter layer displacements or local maxima in the near-bottom water density (Fig. 6). These have timescales $100 \leq \tau \leq 500$ s, vertical displacements $2 \leq a \leq 10$ m, normalized vertical displacement $0.1 \leq a/H \leq 0.7$, and near-bottom density variation $0.5 \leq \Delta\sigma_t \leq 1.5$ kg m^{-3}. In comparison to the observations collected at site *A* the day before at around the same tidal phase (Fig. 4), the bolus signal at site *B* inferred from the density measurements alone is much clearer, although the density variations $\Delta\sigma_t$ are about 4 times weaker (compare the σ_t panels and associated scales of Figs. 4 and 6).

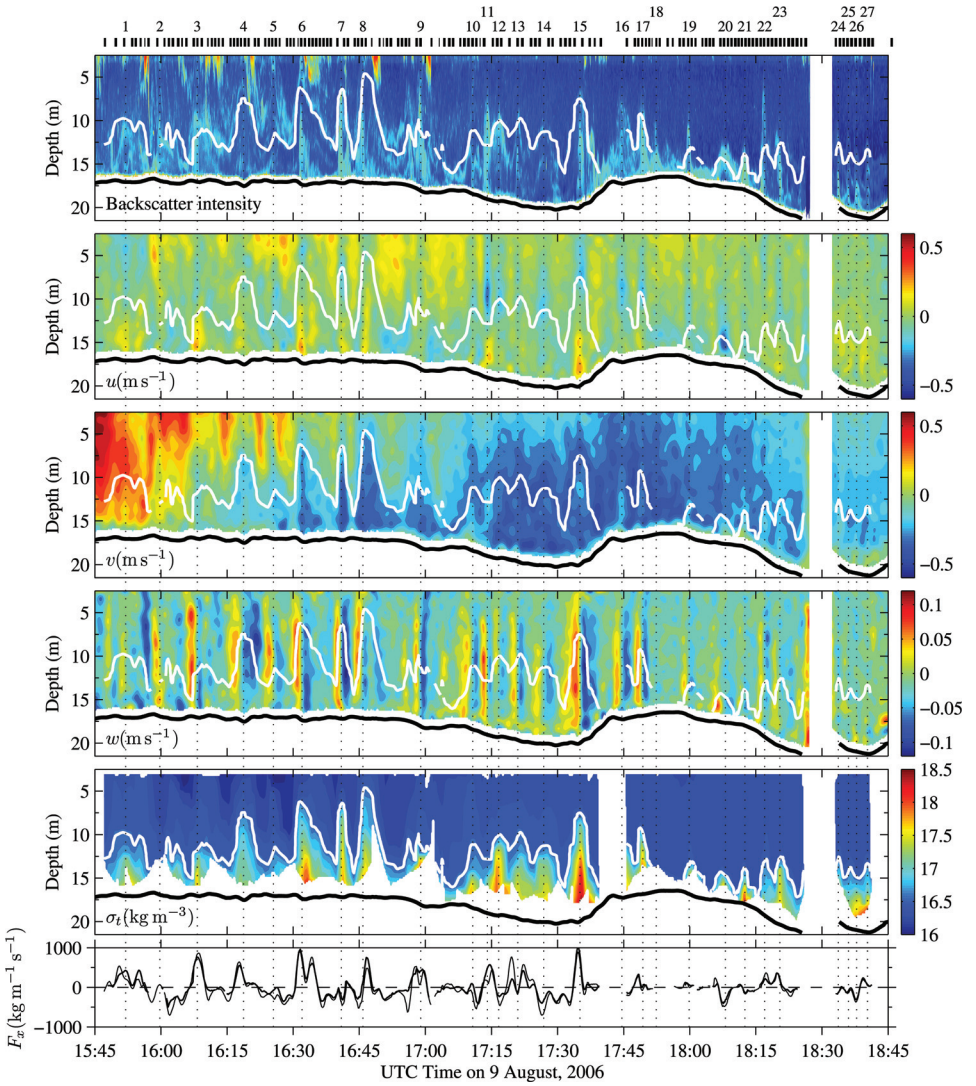

Figure 6. Observations of boundary processes at site *B*. Space-time contours of the (first) backscatter intensity, (second) across-shore u, (third) along-shore v, and (fourth) vertical w currents, (fifth) density σ_t, and (sixth) across-shore transport of sub-slope water F_x. The thin and thick lines in the bottom panel are for, respectiviely, the lower and upper bound used for the reference density ρ_s in the calculation of F_x (see text and Eq. 10). The white contour line in each panel is $\sigma_t = 16.6\,\mathrm{kg\,m^{-3}}$ used for calculating bolus transport (see text). The thick black line is the water bottom as detected by the ADCP. Other symbols are as in Figure 4.

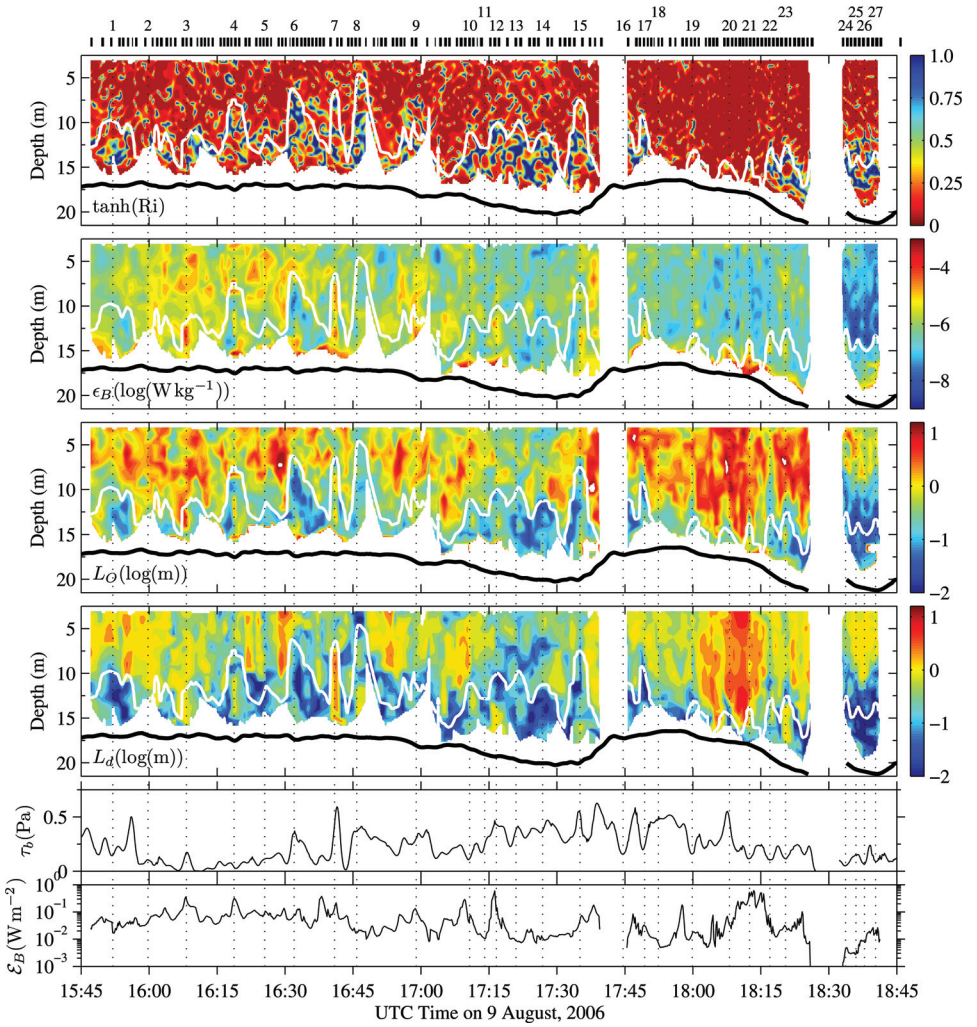

Figure 7. Observations of turbulent processes at site *B*. Space-time contours of the (first) Richardson number tanh(Ri), (second) dissipation rate of turbulent kinetic energy ϵ_B, (third) Ozmidov scale L_O, (fourth) displacement scale L_d, (fifth) bottom stress τ_b and (bottom) dissipation rate area density $\mathcal{E}_B$. Other symbols are as in Figure 6.

Most boluses identified at site *B* were characterized with a clear alternating upward and downward vertical velocity pattern, of magnitude $\mathcal{O}(0.1\ \mathrm{m\,s^{-1}})$, that affected the entire water column. This vertical velocity structure is not as apparent for the smaller-amplitude boluses (boluses $20-27$). Comparing the wave-induced horizontal and vertical velocity scales reveals that the boluses are nonhydrostatic, i.e. $\mathcal{O}(w')/\mathcal{O}(u') \sim 1$.

Measurements at site *B* were collected during the ebb-to-flood reversal of tidal currents (Fig. 6). The low frequency horizontal circulation (U, V) (not shown) was principally oriented along-channel with depth-averaged velocities in the range $-0.03 \leq \overline{U} \leq 0.05\ \mathrm{m\,s^{-1}}$ and $-0.3 \leq \overline{V} \leq 0.4\ \mathrm{m\,s^{-1}}$.

There appears to be significant vertical banding, coincident with the passage of boluses, in the along-channel velocity field v (Fig. 6). This is particularly apparent between 1615 and 1715 UTC. Such fluctuations may be due to wave heaving of vertically-sheared background flows, even for situations where the waves propagate orthogonally to the flow direction (Mirshak, 2008; Mirshak and Kelley, 2008). This is likely the cause for the bands observed here. The bands in v are much less apparent after 1715 UTC when the flow is more barotropic.

ii. Bolus transport. As seen in laboratory experiments (Helfrich, 1992) and numerical simulations (Bourgault *et al.*, 2005; 2007; Mirshak, 2008), shoaling boluses can transport sub-pycnocline water up-slope, on the flank of an island. This can be an important mechanism for bringing up nutrients and cold water in the internal swash zone with potential impact to the local ecosystem (e.g. marine mammals (Bédard *et al.*, 1997)).

The rate F_x, in $\mathrm{kg\,m^{-1}\,s^{-1}}$, at which sub-pycnocline water was being swashed back and forth on the island slope was calculated as

$$F_x = \int_{z_1}^{z_2} u' \rho \delta \, dz + \int_{-H}^{z_1} u' \rho(z_1) \delta \, dz, \tag{10}$$

where

$$\delta = \begin{cases} 1 & \text{if } \rho \geq \rho_s, \\ 0 & \text{otherwise,} \end{cases} \tag{11}$$

$\rho = \sigma_t + 10^3$ is the water density, $\rho_s = 1016.6 \pm 0.1\ \mathrm{kg\,m^{-3}}$ taken as representative of the density of sub-pycnocline water and z_1 and z_2 as defined in Eq. 5. The value for ρ_s was chosen by visual inspection of the density and backscatter fields as the bolus interfacial isopycnal. The $\rho_s = 1016.6\ \mathrm{kg\,m^{-3}}$ isopycnal is depicted with the white contour curve in each panel of Figure 6 and with the thick white contour curve in each panels of Figures 11 to 14. The second integral in the above equation employs extrapolation due to the fact that density measurements were not collected to the bottom $-H$. The method is a zero gradient extrapolation where the deepest measurement, i.e. $\rho(z_1)$, is extended to the bottom. The result of the analysis is not sensitive to this extrapolation. Given the $\pm 0.01\ \mathrm{m\,s^{-1}}$ uncertainty in the current measurements, the uncertainty in F_x is $\pm 10^2\ \mathrm{kg\,m^{-1}\,s^{-1}}$.

The amount of water swashed and backwashed on the slope, as quantified by F_x, is shown in the bottom panel of Figure 6. The figure shows two curves corresponding to

the lower and upper bound used for ρ_s. All quantities derived from F_x in the text below were computed from the average of these two curves. Large boluses (e.g. boluses 3, 4, 5, 8, 9, 15) can transport instantaneously between about $F_x = 5 \times 10^2$ kg m^{-1} s^{-1} and $F_x = 1.0 \times 10^3$ kg m^{-1} s^{-1} of dense water shoreward. However, backwash events (i.e. $F_x < 0$) are also prominent and of the same order or magnitude as swash events. Some backwash events occur between boluses, e.g. between boluses 3 and 4 or between boluses 5 and 6, but other significant backwash events with $F_x \approx -5 \times 10^2$ kg m^{-1} s^{-1}, are coincident with some of the identified boluses. This is particularly clear for boluses 14 and 20. This suggests that internal backwash, i.e. the return down the slope of unmixed dense water previously brought up by shoaling boluses, may manifest itself in the form of downslope bolus-like features. An example of such a downslope bolus will be presented below.

The mean rate of mass swashed/backwashed on the slope is $\overline{F}_x = -0.2 \times 10^2$ kg m^{-1}s^{-1} ≈ 0, given the uncertainty in F_x. This calculation suggests that the amount of dense water brought up the slope during run-up is balanced by the amount of dense water brought down the slope during run-down.

iii. Turbulence. Figure 7 shows quantities that relate to the turbulent field. As at site *A*, dissipation is patchy and highly variable with $\overline{\epsilon}_B = 5 \times 10^{-6}(5 \times 10^{-8}, 2 \times 10^{-5})$ W kg^{-1}, $\overline{\mathcal{E}}_B \geq 0.1(0.007, 0.5)$ W m^{-2}. The turbulence intensity ($\overline{\epsilon}_B$ and $\overline{\mathcal{E}}_B$) at site *B* is roughly 60% higher than that observed at site *A* the day before and at roughly the same tidal phase.

During the 3-hour observing period, the flow is largely dynamically unstable throughout the water column by 80% of the field characterized by Ri $\leq 1/2$ and 70% with Ri $\leq 1/4$ (Fig. 7, top panel). The Richardson number field is patchy and it is not immediately clear whether the passage of boluses altered the stability of the flow. However, close visual inspection reveals that there are more blue patches, i.e. stable conditions, associated with the passage of the boluses inferred from the ρ_s isopycnal displacement (white contour on Fig. 7). This can be assessed more quantitatively by examining the relationship between the fraction $f_{\mathrm{Ri}<1/4}$ of the water column subject to low values ($<1/4$) of the Richardson number and the normalized displacement ζ of the ρ_s isopycnal defined as

$$\zeta = \frac{z(\rho_s) - \min[z(\rho_s)]}{H}. \tag{12}$$

Figure 8 shows the relationship between $f_{\mathrm{Ri}<1/4}$ and ζ. There is a significant negative correlation between these variables with $R = -0.71 (p < 0.01)$. This relationship is somewhat surprising and intriguing. It suggests that boluses bring some stability to the water column. Furthermore large-amplitude boluses bring more stability than smaller amplitude boluses. This is somewhat contrary to the general understanding that internal waves provide a mechanism for inducing greater shear to a background environment and thus for enhancing flow instabilities and turbulence (Bogucki and Garrett, 1993; Moum *et al.*, 2003). Here, the situation is different because boluses not only bring shear but also stratification.

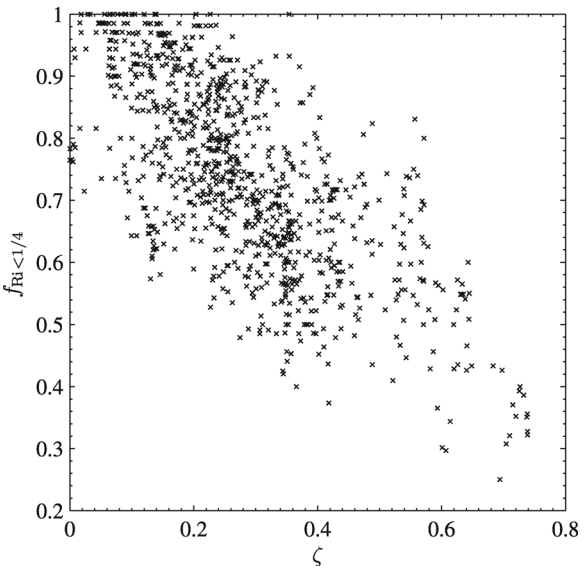

Figure 8. Relationship between the fraction $f_{\mathrm{Ri}<1/4}$ of the water column that is characterized with $\mathrm{Ri} < 1/4$ and the normalized displacement ζ of the interfacial isopycnal ρ_s. The correlation coefficient is $R = -0.71 (p < 0.01)$.

On the other hand, there is no clear visual correspondence between isopycnal displacements and dissipation ϵ_B. Although we found some significant correlation between Richardson number, expressed in terms of the fraction of the water column that is dynamically unstable, and the isopycnal displacement ζ (Fig. 8), we found no equivalent relationship between ζ and $\mathcal{E}_B$ (Fig. 9). Some boluses (e.g. 3, 4, 12) are coincident with local maxima in $\mathcal{E}_B$ but in general this dataset provides no clear indication that the presence of a bolus systematically enhances or inhibits the turbulence level of the water column in this complex estuarine environment. We will come back to this point in the discussion.

As for the observations collected at site *A* (Fig. 4), there is an apparent visual correspondance between Ozmidov scale L_O and displacement scale L_d (Fig. 7). The mean Ozmidov scale is $\overline{L}_O = 0.4(0.02, 3)$ m and is comparable to the mean displacement scale $\overline{L}_d = 0.4(0.01, 3)$ m. Both scales are about twice as small as measured at site *A* the day before. Combining both datasets from sites *A* and *B*, Figure 10 shows the relationship between the depth-averaged Thorpe L_T and Ozmidov $< L_O >$ scales. There is a significant correlation between these variables with $R = 0.75$ ($p < 0.01$). Figure 10 resembles results reported by Peters (1997) for the relationship between 20-min averages Thorpe and Ozmidov scales (his Fig. 14). The mean ratio of these scales, $\overline{(< L_O > / L_T)} = 1.6(0.4, 4.1)$, is comparable to the ratio $\overline{(L_O/L_T)}_{20\,\mathrm{min}} \approx 1.5$ reported by Peters (1997).

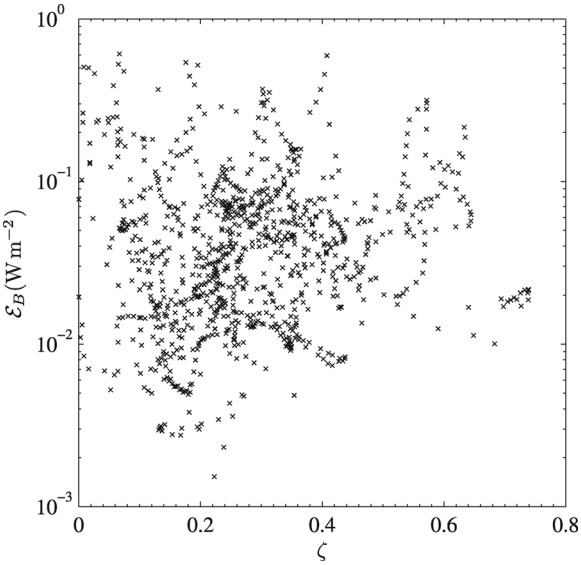

Figure 9. Relationship between $\mathcal{E}_\mathcal{B}$ and the normalized displacement ζ of the interfacial isopycnal ρ_s. The linear correlation coefficient is $R = -0.03$ ($p = 0.4$) between $\mathcal{E}_\mathcal{B}$ and ζ, and $R = 0.11$ ($p < 0.01$) between $\log(\mathcal{E}_\mathcal{B})$ and ζ.

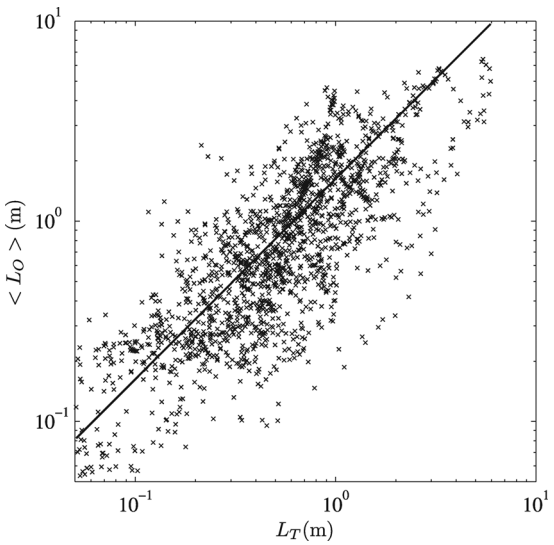

Figure 10. Scatter plot showing the relationship between the depth-averaged Ozmidov $< L_O >$ and Thorpe scales L_T. The correlation coefficient is $R = 0.75$ ($p < 0.01$). The line corresponds to $< L_O >= 1.6 L_T$, where the coefficient is the mean of the lengthscale ratios, i.e. $\overline{< L_O > / L_T} = 1.6$ (see text).

Figure 7 shows the inferred bottom shear stress τ_b. Some boluses coincide with local maxima in bottom shear stress as would be expected for boluses, or internal waves, propagating in an otherwise quiescent environment (e.g. boluses 3, 6, 7, 15, 20). There are, however, just as many cases, if not more, of boluses being coincident with local minima in bottom shear stress (e.g. 10, 16, 17, 19, 21, 22, 23, 24, 26). This is likely due to the superposition of the bolus-induced near-bottom current and comparable flow fluctuations of other origins. In fact, there is little correlation between τ_b and the displacement of the ρ_s isopycnal ζ ($R = 0.1$, $p < 0.01$). The average magnitude and variability of the bottom stress is $\overline{\tau}_b = 0.2(0.01, 0.5)$ Pa. This stress is sufficient to resuspend sand (Houwing and van Rijn, 1998).

c. Bolus structure

Closer inspection of the backscatter intensity reveals that the boluses observed at site *B* are complex features (Fig. 6, top panel). Boluses are characterized with various shapes, they are not ranked in order of amplitude and there is little periodicity in the signal observed. In this section, we present in more detail the structure of a few representative boluses.

i. A large-amplitude symmetrical bolus. Figure 11 shows the structure of bolus 4 (see Figs. 6 and 7). This large-amplitude bolus ($a/H = 0.6$) exhibits an approximately symmetrical shape. The v panel illustrates well the heaving effect discussed earlier of the vertically-sheared background environment caused by the passage of the bolus. The vertical velocity field is consistent with the isopycnal displacement field and with the oscillatory nature of the bolus.

The turbulence structure around this bolus is patchy and highly variable. The highest values of dissipation, in excess of $\epsilon > 10^{-4}$ W kg^{-1}, are found around the bolus crest (i.e. around the thick white contour line) and near the bottom center of the bolus. The high dissipation observed near the crest may be due to shear instability caused by the combined action of bolus-induced and background shear, consistent with low Richardson number at that location. However, given the patchiness of the dissipation field, it could also be simply coincidental that this patch appears near the bolus crest. In general, there is no clear correspondence between the isopycnal displacements and the dissipation field.

Coincident with the bolus-induced downwelling, just behind the bolus crest (between 1619 and 1621 UTC), there is enhanced backscatter intensity near the surface (colored yellow - red in the figure). In the field, this was coincident with choppy surface waters. Surface manifestations of internal waves and boluses can be regularly observed in this area and are used as an aid for localizing such features during sampling (see for example the shore-based photography of Bourgault and Kelley (2003)).

ii. A large-amplitude asymmetrical bolus. Figure 12 shows the structure of bolus 6 (Figs. 6 and 7). This bolus is also characterized with large amplitude $a/H = 0.6$. Unlike the previous example, it is asymmetrical, with its front face being about 5 times steeper than its rear face.

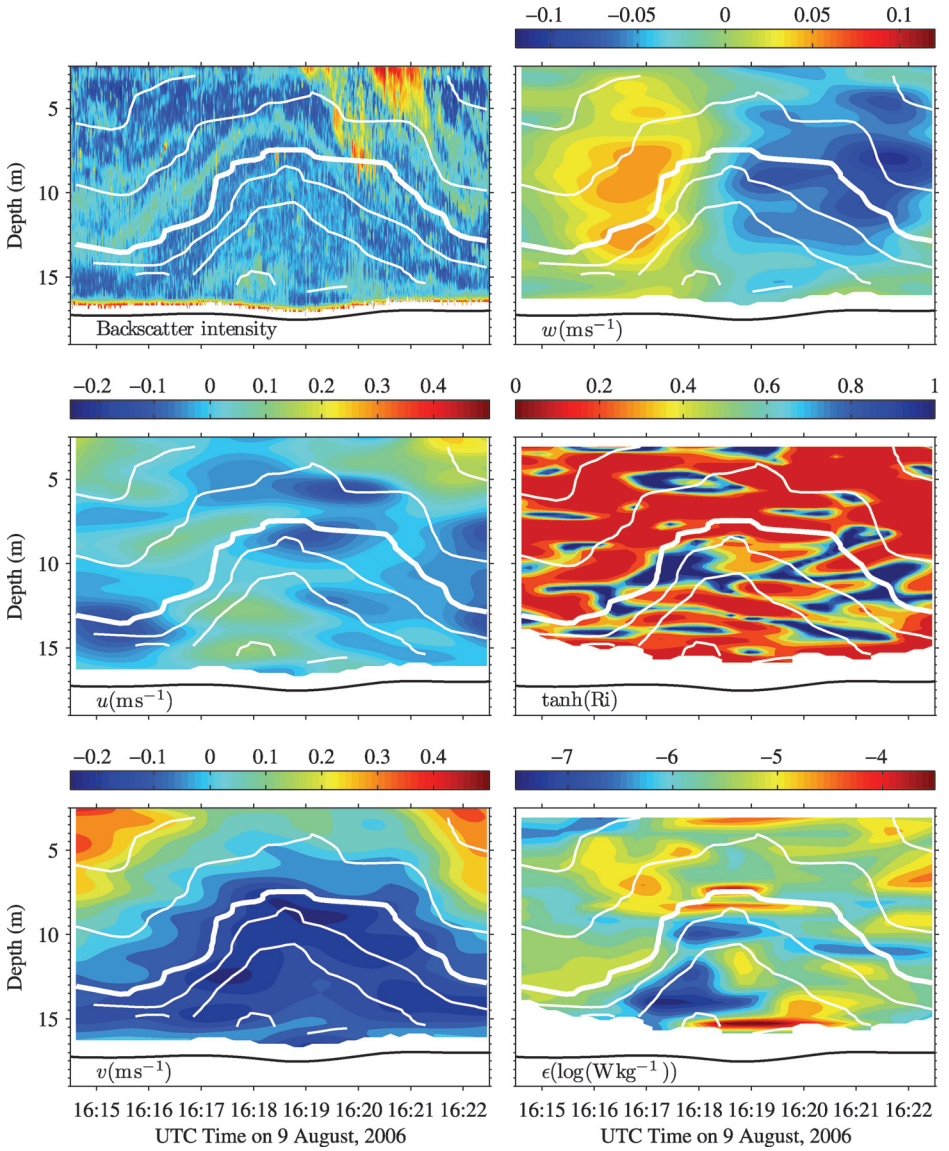

Figure 11. The structure of a large-amplitude symmetrical shoaling bolus (bolus 4 on Figure 6). The white lines in each panel are density countours, 0.2 $\mathrm{kg\,m}^{-3}$ apart and the thick white line is the $\sigma_t = 16.6\ \mathrm{kg\,m}^{-3}$ used for the calculation of F_x (see text and Eq. 10).

This asymmetry in the bolus shape suggests that it may be advectively unstable, such that it is about to plunge and terminate abruptly, as hypothesized by Klymak and Moum (2003) for waves of elevation shoaling on the Oregon Shelf. However, the field observations of Bourgault *et al.* (2007) do not reveal plunging events for such asymmetrical boluses. These

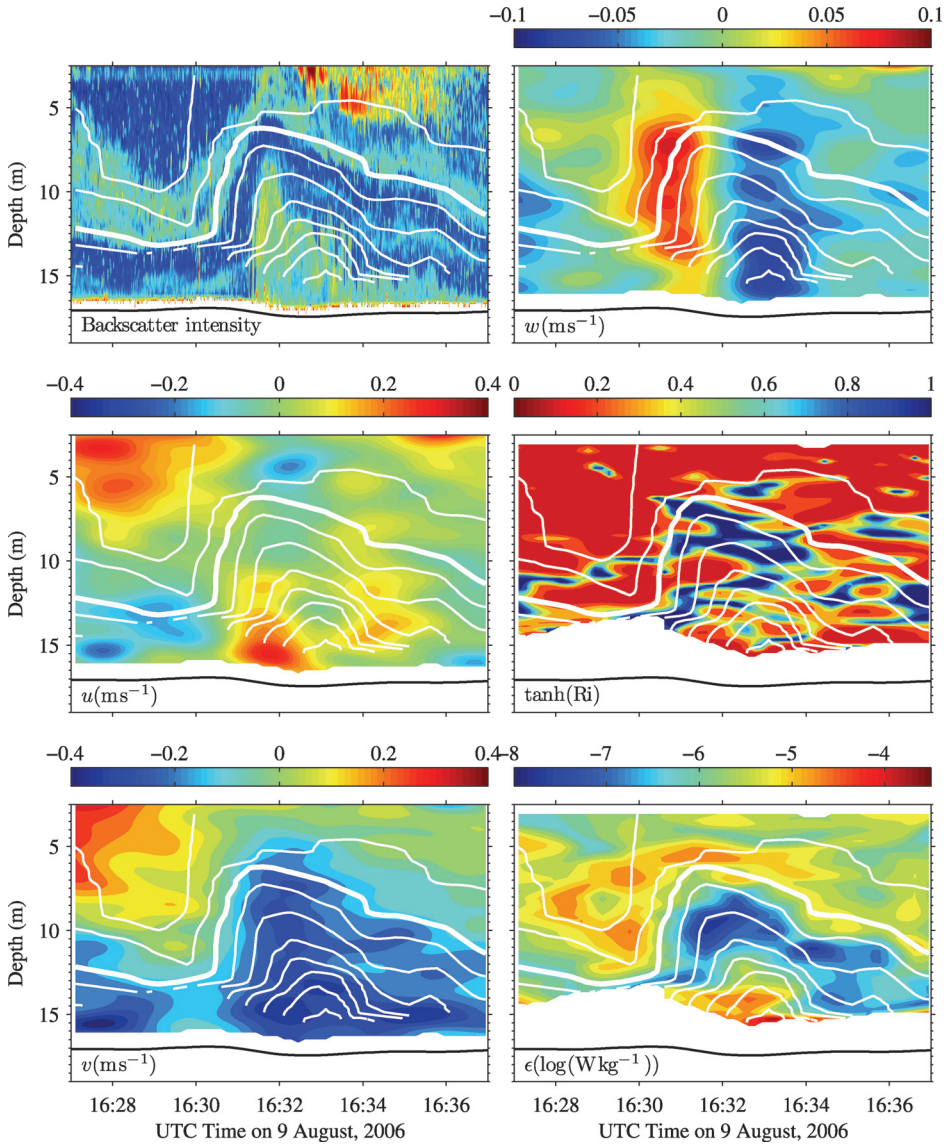

Figure 12. The structure of a large-amplitude asymmetrical shoaling bolus (bolus 6 on Figure 6). All symbols and lines are as in Figure 11.

boluses tend to preserve their asymmetrical shape during their upslope evolution. Perhaps the bolus is indeed advectively unstable and breaks more like a spilling breaker where the scale of the breaking is too small to be observed with echo-sounders.

The bolus-induced horizontal velocity structure is clearer for this case than the previous example, although the environment is also characterized with complex motions of similar

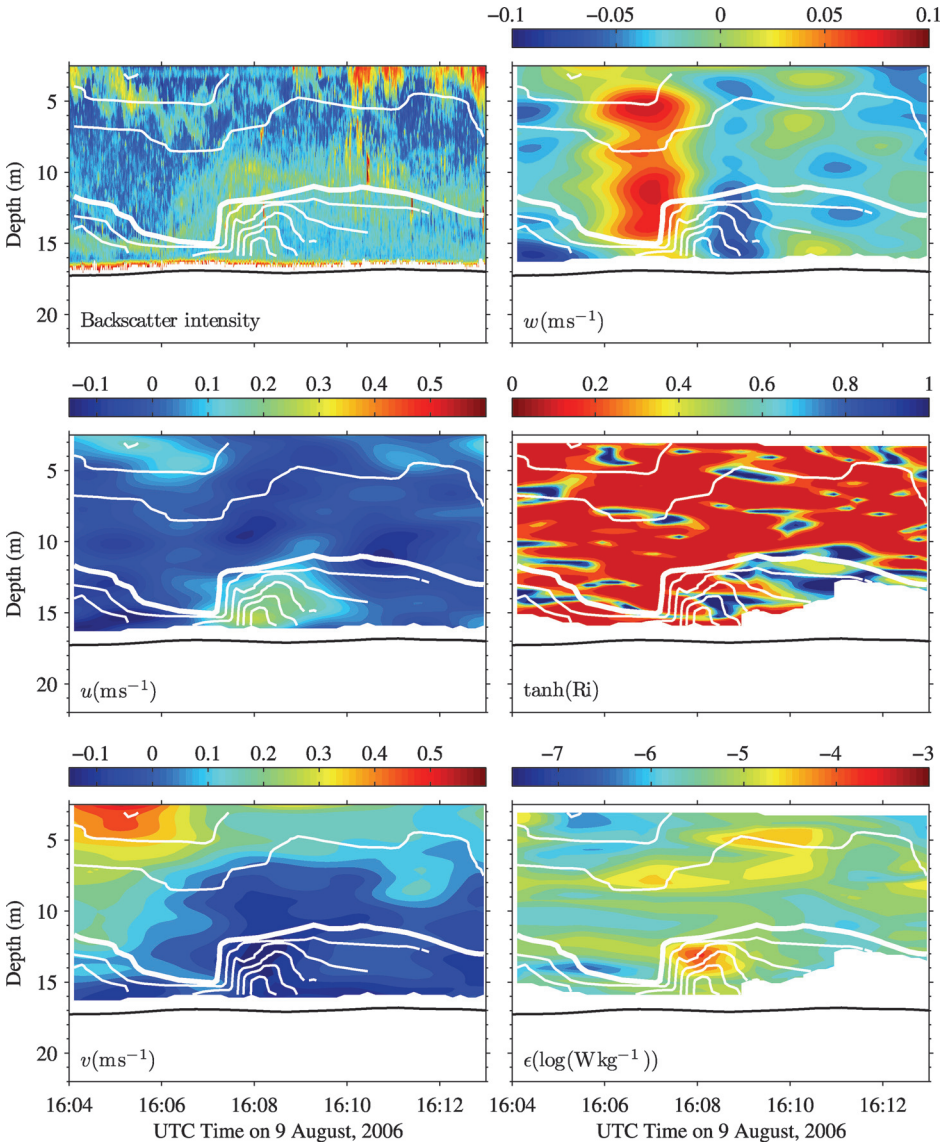

Figure 13. The structure of an moderate-amplitude front-like bolus (bolus 3 on Figs. 6 and 7). All symbols and lines are as in Figure 11.

scale and magnitude. There is a clear core underneath the interface with shoreward velocity $u \approx 0.2\ \mathrm{m\,s^{-1}}$. Here also, heaving by the bolus of the background vertically-sheared environment is clear in the v field.

The pattern of the dissipation field exhibits here some similarities with the backscatter and isopycnal displacement fields. Comparing the backscatter intensity field with the turbulent

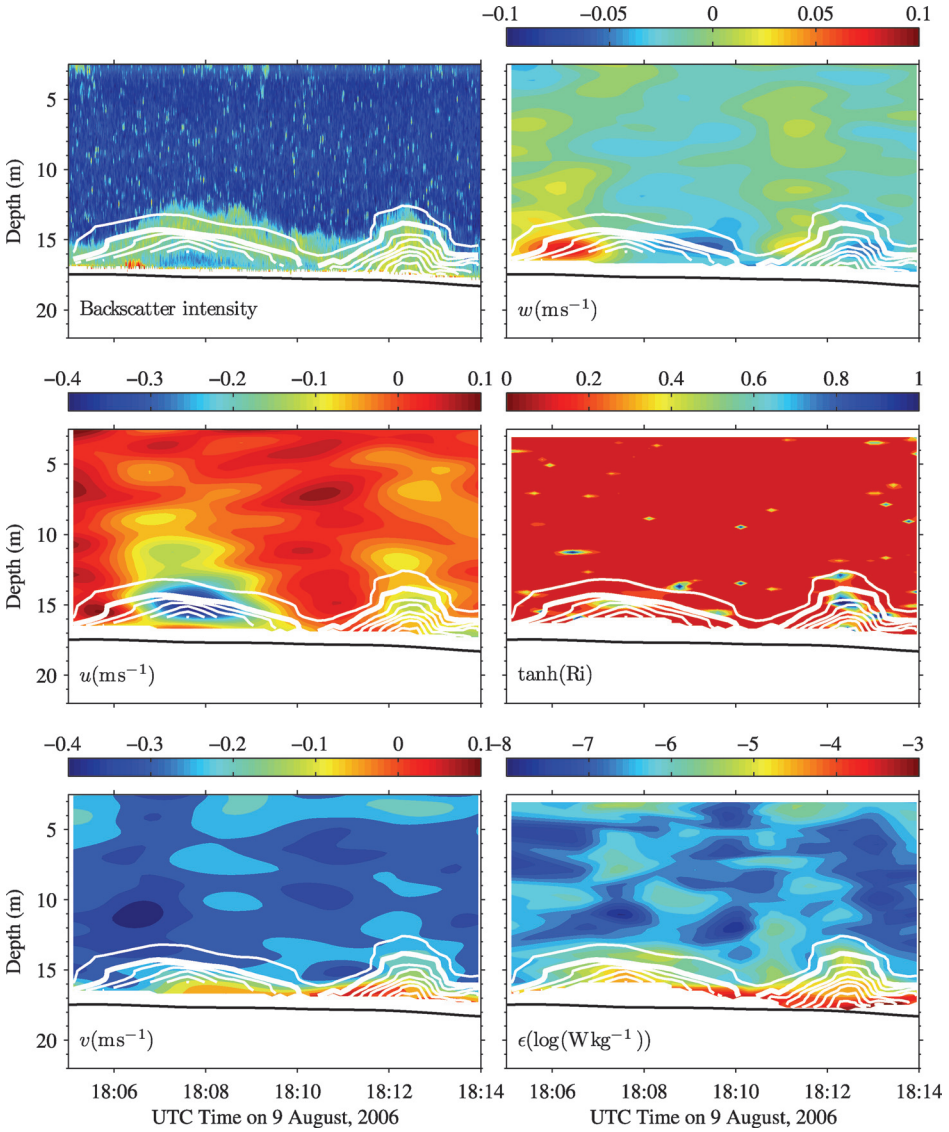

Figure 14. The structure of a small-amplitude offshore-propagating boluses (bolus 20 and 21 on Fig. 6). All symbols and lines are as in Figure 11.

dissipation field suggests that the 3-m thick near-bottom layer just ahead of the bolus, between 1627 and 1630 UTC, is characterized by low turbulent dissipation rates. As this bolus passes, it displaces the isocpynals and scattering layers upward by approximately 7 m, displacing the low-turbulence layer upward without making it more turbulent, with dissipation of order 10^{-8} to 10^{-7} W kg^{-1} between 8 m and 11 m and 1631 and 1634 UTC.

This low turbulence layer overlies the center of the bolus with a much more turbulent layer of order 10^{-5} W kg^{-1}. It cannot be unambiguously determined whether this high turbulence is inherent to the bolus core or whether it is the turbulent bottom boundary layer that is being heaved upward by the bolus to a depth sampled with our turbulence profiler.

As in the previous example, enhanced backscatter intensity is observed near the surface and just behind the bolus crest. This was coincident with enhanced sea-surface roughness. The passage of this bolus was anticipated from visual observations of the sea surface while we sampled.

iii. A moderate-amplitude bore-like bolus. Some boluses are not characterized by well-defined shapes. Figure 13 shows an example of a bore-like bolus, with a steep front followed by a long tail. The vertical displacement at the front $a/H = 0.3$ is moderate compared to the amplitude of the previous two cases discussed above. Near-surface enhanced backscatter intensity is seen behind the bolus head. This bolus was expected during field sampling from its surface signature.

This bolus is one of the few cases that shows a well-contained and highly turbulent core, with dissipation rates of order 10^{-4} W kg^{-1}, associated with the head of the bolus. Other cases examined in this section (previous two cases and the one that follows) also show high dissipation rates surrounding boluses but it is often ambiguous whether the turbulence is part of the background environment or inherent to the bolus.

Just ahead and within the bolus core, the Richardson number suggests dynamically unstable conditions (Ri $< 1/2$). Behind the head and in the tail, the water column appears much more stable. There is also clear vertical spreading of the isopycnals as this bolus propagates, which can be an indication that mixing is taking place.

iv. Small-amplitude downslope propagating bolus. As can be seen in Figure 6, bolus crests do not always coincide with shoreward transports F_x of sub-pycnocline water. This suggests that some of the identified bolus-like features are not shoaling but rather propagate downslope. Boluses 20 and 21, shown in greater detail in Figure 14, are the clearest examples of two of those downslope boluses.

These boluses are characterized by small amplitudes, $a/H = 0.2$, compared to most boluses observed in this experiment. The core of bolus 20 is characterized by negative across-shore horizontal velocity reaching $u \approx -0.4$ m s^{-1}. Bolus 21 does not exhibit such a strong signal in u but the direction is also downslope. Both boluses have vertical velocity signals w consistent with the isopycnal displacements.

There is no enhanced backscatter intensity near the surface associated with these boluses. These small-amplitude near-bottom features passed unnoticed when we sampled them.

The background environment in which these boluses evolve is largely unstable as revealed by the uniformly low Richardson number values throughout the water column. The boluses bring some localized stability just below the interface as they pass. These small amplitude boluses are coincident with large near-bottom dissipation, up to 10^{-3} W kg^{-1}. However,

our sampling did not reach all the way to the bottom, so it cannot be concluded from this incomplete set of observations that the high level of dissipation coincident with these boluses can be attributed to the boluses themselves. An alternative hypothesis is that the bottom boundary layer was turbulent and that the boluses heaved the boundary layer upward.

4. Discussion and conclusions

We have observed a series of large- and small-amplitude internal boluses propagating on an internal beach of the St. Lawrence Estuary. The observations reveal a complex picture of wave-induced boundary processes in the internal swash zone. In particular, the asymmetrical shape, non-periodic and unordered nature of the boluses observed in this study differs remarkably from reported cases of symmetrical shoaling waves of elevation and other bore-like features observed in other coastal systems (Klymak and Moum, 2003; Scotti and Pineda, 2004; Moum *et al.*, 2007) and from simulated boluses generated at shelf breaks (Venayagamoorthy and Fringer, 2007). We also observed a few intriguing cases of small-amplitude bolus-like near-bottom features propagating offshore. The origin of these offshore-propagating boluses is unclear but they may have resulted during internal backwash by a mechanism yet to be identified.

The turbulence observed in the internal swash zone over three-hour periods is high and highly variable with average dissipation rates of $\bar{\epsilon} = 4 \times 10^{-6} (4 \times 10^{-8}, 2 \times 10^{-5})$ $\mathrm{W\,kg^{-1}}$, taking both sample sites into consideration. Our observations are too sparse to determine with confidence what fraction of this dissipation is caused by the boluses relative to other sources such as tidal bottom stress or shear instability of the mean estuarine circulation.

We found one indication that the source of the turbulence may not primarily be the boluses themselves. This is suggested by the link found between increased water column stability and bolus arrivals (Fig. 8). This result would suggest that boluses are dynamically stable structures that can bring more stratification than shear to the slope and may thus contribute to reduced boundary turbulence. Somewhat puzzlingly, we found no significant correlation between bolus arrivals and water column dissipation (Fig. 9). Our dataset indicates that boluses can either be coincident with local maxima or minima in water column dissipation. It is important to re-emphasize that our dataset is incomplete in that turbulence measurements were not collected down through the bottom boundary layer. This can lead to orders of magnitude underestimation of the depth-integrated water column dissipation (see for example a similar discussion in Peters and Bokhorst (2000)). Another consequence of this incomplete sampling, as previously pointed out when discussing the near-bottom turbulence structure of boluses (Figs. 14 and 12), is that it cannot be determined whether high near-bottom dissipation coincident with a bolus is inherent to the bolus or reflects turbulent bottom boundary layers being heaved upward by the bolus. For this reason, we cannot conclude based on the present dataset whether or not boluses are an important source of boundary turbulence.

More research and field observations are required before we could satisfactorily test Mirshak's (2008) hypothesis on the weak-mixing nature of boluses and before we can fully appreciate, quantify and predict the impact of shoaling internal waves on coastal oceanography. Particularly important in the design of future field experiments is to obtain turbulence measurements over longer periods of time than done here and through the bottom boundary layer. These are the main limitations preventing us from making firmer conclusions on the role of boluses in boundary turbulence and coastal oceanography. Nevertheless, this study provides new insights into the structure and behaviour of naturally-occurring boluses and into boundary processes taking place into an internal beach of an estuary.

Acknowledgments. We thank Daniel Thibault and Rémi Desmarais for the instrument preparation, for piloting the boat and for their help during sampling. We are also thankful to the anonymous reviewers and Eric Kunze for their constructive comments. This work was supported by the Canadian Foundation for Climate and Atmospheric Sciences, the Canada Foundation for Innovation, the Natural Sciences and Engineering Research Council of Canada, and the Department of Fisheries and Oceans of Canada.

REFERENCES

Bédard, J., A. Nadeau, J.-P. L. Savard, and M. C. S. Kingsley. 1997. La passe de l'Ile aux Lièvres: importance stratégique pour la faune marine de l'estuaire. Technical Report 283, Environment Canada, Canadian Wildlife Service.

Bogucki, D. and C. Garrett. 1993. A simple model for shear-induced decay of an internal solitary wave. J. Phys. Oceanogr., *23*, 1767–1776.

Bourgault, D., M. Blokhina, R. Mirshak, and D. E. Kelley. 2007. Evolution of a shoaling internal solitary wavetrain. Geophys. Res. Lett., *34*, L03601, doi:10.1029/2006GL028462.

Bourgault, D. and D. E. Kelley. 2003. Wave-induced boundary mixing in a partially mixed estuary. J. Mar. Res., *61*, 553–576.

Bourgault, D., D. E. Kelley, and P. S. Galbraith. 2005. Interfacial solitary wave run-up in the St. Lawrence Estuary. J. Mar. Res., *63*, 1001–1015.

Dillon, T. M. 1982. Vertical overturns: a comparison of Thorpe and Ozmidov length scales. J. Geophys. Res., *87*(C12), 9601–9613.

Galbraith, P. S. and D. E. Kelley. 1996. Identifying overturns in ctd profiles. J. Atmos. Oceanic Technol., *13*, 688–702.

Gargett, A. E. and T. Garner. 2008. Determining thorpe scales from ship-lowered ctd density profiles. J. Atmos. Oceanic Technol., *25*, 1657–1670.

Geyer, W. R., J. H. Trowbridge, and M. M. Bowen. 2000. The dynamics of a partially mixed estuary. J. Phys. Oceanogr., *30*, 2035–2048.

Gill, A. E. 1982. Atmosphere-Ocean Dynamics, Academic, San Diego, CA, 662 pp.

Gregg, M. C. 1999. Uncertainties and limitations in measuring ϵ and χ_t. J. Atmos. Oceanic Technol., *16*, 1483–1490.

Helfrich, K. R. 1992. Internal solitary wave breaking and run-up on a uniform slope. J. Fluid Mech., *243*, 133–154.

Houwing, E.-J. and L. C. van Rijn. 1998. *In Situ* Erosion Flume (ISEF): determination of bed-shear stress and erosion of a kaolinite bed. J. Sea. Res., *39*, 243–253.

Jackson, C. R. 2004. An atlas of internal solitary-like waves and their properties. Second Edition. Technical Report Code 322PO, Contract N00014-03-C-0176, Office of Naval Research. http://www.internalwaveatlas.com.

Klymak, J. M. and M. C. Gregg. 2004. Tidally generated turbulence over the Knight Inlet sill. J. Phys. Oceanogr., *34*, 1135–1151.

Klymak, J. M. and J. N. Moum. 2003. Internal solitary waves of elevation advancing on a shoaling shelf. Geophys. Res. Lett., *30*, 2045, doi:10.1029/2003GL017706.

Kundu, P. K. and I. M. Cohen. 2004. Fluid Mechanics, Third Edition, Elsevier Academic Press, San Diego, 759 pp.

Lewis, E. L. and R. G. Perkin. 1978. Salinity: Its definition and calculation. J. Geophys. Res., *83* (C1), 466–478.

Lueck, R., F. Wolk, and H. Yamazaki. 2002. Oceanic velocity microstructure measurements in the 20th century. J. Oceanogr., *58*, 153–174.

Macoun, P. and R. Lueck. 2004. Modeling the spatial response of the airfoil shear probe using different sized probes. J. Atmos. Oceanic Technol., *21*, 284–297.

Michallet, H. and G. N. Ivey. 1999. Experiments on mixing due to internal solitary waves breaking on uniform slopes. J. Geophys. Res., *104* (C6), 13467–13477.

Miles, J. 1961. On the stability of heterogeneous shear flows. J. Fluid Mech., *10*, 496–508.

Mirshak, R. 2008. Interfacial Internal Waves Impacting Sloped Boundaries, PhD thesis, Dalhousie University, Halifax, Nova Scotia, Canada.

Mirshak, R. and D. E. Kelley. 2008. Inferring propagation direction of nonlinear internal waves in a vertically sheared background flow. J. Atmos. Oceanic Technol., doi:10.1175/2F2008JTECHO632.1 (in press).

Moum, J. N., D. M. Farmer, W. D. Smyth, L. Armi, and S. Vagle. 2003. Structure and generation of turbulence at interfaces strained by internal solitary waves propagating shoreward over continental shelf. J. Phys. Oceanogr., *33*, 2093–2112.

Moum, J. N., M. C. Gregg, R. C. Lien, and M. E. Carr. 1995. Comparison of turbulence kinetic energy dissipation rate estimates from two ocean microstructure profilers. J. Phys. Oceanogr., *12*, 346–366.

Moum, J. N., J. M. Klymak, J. Nash, A. Perlin, and W. D. Smyth. 2007. Energy transport by nonlinear internal waves. J. Phys. Oceanogr., *37*, 1968–1988.

Oakey, N. S. 1982. Determination of the rate of dissipation of turbulent energy from simultaneous temperature and velocity shear microstructure measurements. J. Phys. Oceanogr., *12*, 256–271.

Oakey, N. S. and J. A. Elliott. 1982. Dissipation within the surface mixed layer. J. Phys. Oceanogr., *12*, 171–185.

Ozmidov, R. V. 1965. On the turbulent exchange in a stably stratified ocean. Ivz. Acad. Sci. USSR, Atmos. Oceanic Phys., *1*, 853–860.

Peters, H. 1997. Observations of stratified turbulent mixing in an estuary: neap-to-spring variations during high river flow. Est. Coastal Shelf Sci., *45*, 69–88.

Peters, H. and R. Bokhorst. 2000. Microstructure observations of turbulent mixing in a partially mixed estuary. Part I: Dissipation rates. J. Phys. Oceanogr., *30*, 1232–1244.

RD Instruments. 1996. Acoustic Doppler current profiler, Principles of operations, A practical primer. Technical report, RD Instruments.

Scotti, A. and J. Pineda. 2004. Observation of very large and steep internal waves of elevation near the Massachusetts coast. Geophys. Res. Lett., *31* (L22307, doi:10.1029/2004GL021052).

Thorpe, S. A. 1977. Turbulence and mixing in a Scottish loch. Philosophical Trans. of the Roy. Soc. London A, 125–181.

Venayagamoorthy, S. K. and O. B. Fringer. 2007. On the formation and propagation of nonlinear internal boluses across a shelf break. J. Fluid Mech., *577*, 137–159.

Vlasenko, V. and K. Hutter. 2002. Numerical experiments on the breaking of solitary internal waves over a slope-shelf topography. J. Phys. Oceanogr., *32*, 1779–1793.
Wallace, B. C. and D. L. Wilkinson. 1988. Run-up of internal waves on a gentle slope in a two-layered system. J. Fluid Mech., *191*, 419–442.
Wesson, J. C. and M. C. Gregg. 1994. Mixing at Camarinal sill in the strait of Gibraltar. J. Geophys. Res., *99*(C5), 9847–9878.

Received: *28 May, 2008*; revised: *25 November, 2008*.